Nanoscale

PAPER

View Article Online
View Journal | View Issue

Cite this: *Nanoscale*, 2016, **8**, 2227

On-chip discrimination of orbital angular momentum of light with plasmonic nanoslits†

Shengtao Mei,‡[a,d] Kun Huang,‡[b] Hong Liu,‡[b] Fei Qin,‡[a] Muhammad Q. Mehmood,[a] Zhengji Xu,[c] Minghui Hong,[a] Daohua Zhang,[c] Jinghua Teng,[b] Aaron Danner[a] and Cheng-Wei Qiu*[a,d]

Received 23rd October 2015,
Accepted 24th December 2015

DOI: 10.1039/c5nr07374j

www.rsc.org/nanoscale

The orbital angular momentum (OAM) of light can be taken as an independent and orthogonal degree of freedom for multiplexing in an optical communication system, potentially improving the system capacity to hundreds of Tbits per second. The high compactness and miniaturization of devices required for optical communications impose strict requirements on discriminating OAM modes of light at a small (micro- or even nano-meter) scale for demultiplexing; these requirements represent a challenge for traditional OAM sorting strategies. Here, we propose a semi-ring plasmonic nanoslit to directly and spatially sort various OAM modes of light into ~120 nm-spaced mode intervals on the metallic surface. Making use of the constructive interference of a helical-phase modulated surface wave excited by a vortex beam, this on-chip interval can be stably demonstrated both theoretically and experimentally with a quasi-linear dependence on the plasmonic wavelength. Furthermore, its immunity to semi-ring geometry (*i.e.*, the radius and number of rings) is verified by simulations. As a result, OAM discriminating is guaranteed by this stable sorting function. This technique shows a viable solution to discriminate the OAM of light at the nano-scale and might lead to broad benefits across the fields of optical communications, plasmonic physics and singular optics.

It was discovered by Allen *et al.* that the orbital angular momentum (OAM) modes of light are associated with an optical vortex having a helical or twisted wavefront of $\exp(il\phi)$, where ϕ is the azimuthal angle and l is the topological charge of vortex.[1] The most famous vortex beam with a well-defined OAM of $l\phi$ (ϕ is the reduced Planck constant) is the Laguerre–Gaussian beam that possesses a series of optical orthogonal eigenmodes, which has been used to demonstrate high-dimension quantum entanglement by violations of Bell-type inequalities.[2,3] In addition, because of the orthogonality of eigenmodes, the OAM of light introduces a new degree of freedom for multiplexing to enhance the capacity of data transmission systems up to hundreds of Tbits per s in optical communications.[4–7] However, devices in optical communications are usually expected to have a small volume for integration purposes,[8–13] and nanophotonic applications are always based on nano-scale designs.[14–18] This imposes a stringent requirement on the challenging fact that these OAM modes at the terminal of a communication system have to be demultiplexed into highly-confined separated spots simultaneously, with a micro- or nano-scale spatial interval between two neighboring modes.

Traditional strategies of sorting OAM modes with bulk optical elements, including the interferometric method,[19,20] thermally tuned q-plates,[21] log-polar coordinate transformation,[22–28] and mimicking Faraday rotation,[29] arrive at either a large-scale spot for each OAM state, or the separation of neighboring OAM modes with a large interval. However, the reported miniaturized devices for OAM sorting suffer from either allowing only indirect measurement *via* special interference patterns[30] or a limited sorting range.[31,32] Therefore, it is urgent to demonstrate a nano-sorter of OAM for demultiplexing in a highly integrated optical communication terminal.

Here, we report a semi-ring shaped nanoslit to serve as a robust and direct OAM sorter that is able to map the OAM modes of light into different subwavelength spots with an on-chip spatial interval of 120 nm (at a visible wavelength of

[a]*Department of Electrical and Computer Engineering, National University of Singapore, 4 Engineering Drive 3, Singapore 117583, Singapore. E-mail: chengwei.qiu@nus.edu.sg*
[b]*Institute of Materials Research and Engineering Agency for Science, Technology and Research (A*STAR), #08–03, 2 Fusionopolis Way, Innovis, Singapore 138634*
[c]*Nanophotonics Laboratory, School of Electrical and Electronic Engineering, Nanyang Technological University, Singapore 639798, Singapore*
[d]*Graduate School for Integrative Sciences and Engineering, National University of Singapore, Centre for Life Sciences (CeLS), #05-01, 28 Medical Drive, Singapore 117456, Singapore*
†Electronic supplementary information (ESI) available. See DOI: 10.1039/c5nr07374j
‡These authors contributed equally to this work.

633 nm) between neighboring states. This is achieved by illuminating a circularly polarized vortex beam on the nanoslit to excite and imprint surface plasmon polaritons (SPPs) with a helical wavefront, so that these phase-modulated plasmons are focused into spatially separated subwavelength spots[33,34] for different vortices due to constructive interference. The high immunity inherent in the ring geometry makes this approach a viable solution for on-chip discrimination of OAM in many applications such as optical communications and integrated optics.

To demonstrate this mechanism, we show different cases for sources having angular-dependent phase modulation in Fig. 1a. Its accumulated phase difference $\Delta\psi$ along the azimuthal direction is defined as $\Delta\psi = \int_{-\pi}^{0} \frac{\partial P(\phi)}{\partial \phi} d\phi$, where $P(\phi)$ is the modulated phase of the semi-circular source. In particular, we consider that $P(\phi)$ has a linear dependence on the angle coordinate ϕ because the helical phase of OAM[35,36] exactly exhibits such a required distribution. The employment of OAM is, of course, only one exemplary strategy to yield such a modulated phase. Fig. 1a schematically shows transversely shifted focal spots with different locations for $\Delta\psi$ = 0, 2π, 6π and 10π, which implies that the modulation depth of the accumulated phase of the semi-circular source can be indirectly inferred by addressing its corresponding focal position. As a result, this system can be used as an on-chip nano-sorter to discriminate the OAM of light when a vortex beam is illuminated upon such plasmonic nanoslits. In addition, one single plasmonic source (*i.e.*, nanoslits) in the metallic film will increase the difficulties in experimental measurement because of the high propagation loss of surface wave so that we adopt five sources to enhance the focal intensity in our experiment, as shown in Fig. 1b.

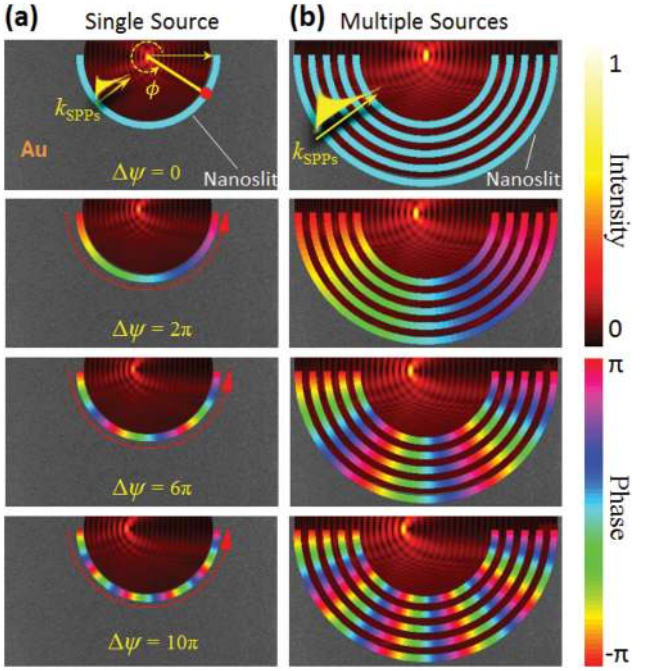

Fig. 1 Focal shifts of a semi-circular plasmonic lens after being imprinted with an azimuthal phase. (a) This plasmonic lens is made of a transparent nanoslit that excites the surface wave, forming a semi-circular plasmonic source in the gold film. Wavelets from this semi-circular source constructively interfere near the original point of the circular source resulting in a well-confined focal spot that will shift when a semi-circular source is imprinted with an azimuthal (ϕ) phase. (b) Multiple semi-circular sources to enhance the focal spot intensity for easy measurement in experiments.

Fig. 2 shows the mechanism, FDTD simulation, and analytical model to describe the focal spot shifting phenomenon quantitatively. The secondary wavelets on the slit constructively interfere at a certain position along a line radial to the slits to form a focal point. On the basis of the Huygens–Fresnel principle, we are able to track the surface wave field distribution within the semi-ring shape slits. Considering that the incident light has an electric field of $E \propto e^{iP(\phi)}e^{-r^2}$ with a radially polarized state, the electric field at the surface is given by:

$$U(\vec{r}) = \int_{-\pi}^{0} \exp(iP(\phi)) \frac{\exp(ik_{SPP}|\vec{R} - \vec{r}|)}{\sqrt{|\vec{R} - \vec{r}|}} d\phi, \quad (1)$$

where $\vec{R}$ is the position vector of any point on a semi-ring slit, $\vec{r}$ denotes the position vector of any viewpoint F, and the original point O is located at the center of the semi-circular slit, as depicted in Fig. 2a. Given that the initial phase is merely induced by OAM ($P(\phi) = l\phi$, l is the topological charge of OAM), using eqn (1), we show the intensity profile for different OAM modes (l = 0, 1, 2, 3, 4) calculated by the analytical model in Fig. 2b, which unambiguously demonstrates separated focal points along the x direction (*i.e.*, the base of the semicircle). Light beam with l = 0 (Gaussian beam) will be focused at the original point O, and the rest will be located in order on the left side. On the other hand, it is expected that all the negative l will be focused on the right side of the center because of symmetry breaking along the azimuthal direction by the semi-ring shaped slit. Larger $|l|$ leads to a bigger transverse shift. Obviously, the number of the sortable OAM states is limited only by the SPP propagation loss, which is a big advantage when it comes to real applications compared with previously reported integrated sorters.

More importantly, all the focal points have a subwavelength size in the x direction and are separated in a nearly uniform way with a subwavelength on-chip interval. Due to this small interval compared to the ring diameter, we can further simplify the expression for the electric field along x as $U(x) = J_l(k_{SPP}x)$ by employing the paraxial approximation to eqn (1), such that the position at the peak focal point can be analytically expressed by:

$$\chi_l = \mathrm{sgn}(l)\chi_l / k_{SPP}, \quad (2)$$

where χ_l is the first non-null zero point of $J'_l(x)$ (the derivative of $J_l(x)$) for $l \neq 0$ and $\chi_{l=0} = 0$. This means that the focal positions are totally determined by the topological charge l and the wavelength λ_{SPP} of SPPs. In order to verify our analytical model, we simulate the nanoslit shown in Fig. 2a at a wavelength of 633 nm through FDTD. The simulated intensity profile along x is shown to have a great agreement with our

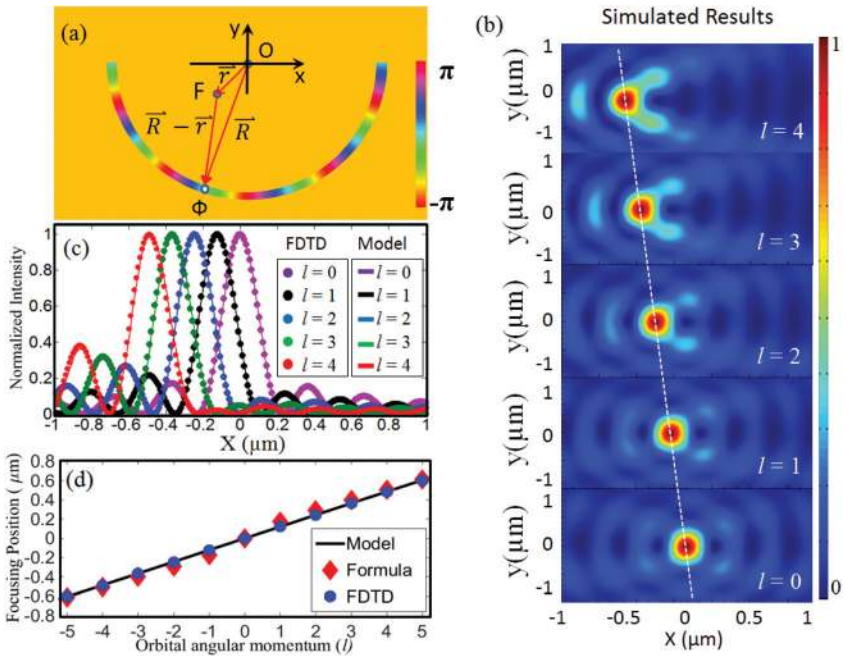

Fig. 2 Mechanism, FDTD simulation, and analytical model of the nano-sorter under radially polarized LG beam illumination. (a) Mechanism of the nano-sorter. (b) Simulated focusing positions of different OAM modes using an analytical model. (c) Field distribution fitting by the FDTD simulation (dots) and analytical model (solid lines). (d) Comparison of focusing positions between the analytical model (solid line), FDTD (blue dots), and the derived focusing position formula (red diamonds).

analytical predictions, which can be observed from Fig. 2c. In addition, the distance between any two neighboring OAM modes is about 120 nm and the lateral (along x) spot size is about 200 nm, which demonstrates a distinguishable separation for different OAM modes. Here we stress that the side band in Fig. 2c actually does not increase monotonously with the topological charge as shown in Fig. 1S in the ESI.† This provides a feasible solution for sorting the OAM modes of light at the nano-scale. We also display the position x_l of peak intensity of hotspots for different OAM modes with a straightforward comparison among FDTD simulation, theoretical model and the analytical formula of eqn (2), as shown in Fig. 2d. The quasi-linear dependence of x_l on the angular momentum makes our nano-sorter viable for precise discrimination of different OAM modes in real cases. The consistence among the three approaches shows that eqn (2) excels in the prediction of the spatial shift of hotspots with a simpler form.

So far, the above analysis of on-chip OAM discrimination has been based on a single slit without any parameter specification, especially its wavelength independence, which is always considered as a limiting factor. Consequently, a single slit can function as a broadband OAM nano-sorter as long as the incident light's wavelength is smaller than the width of the slit such that SPPs can be excited. As mentioned in Fig. 1, in experiments, the employment of a periodic arrangement of slits, instead of a single slit, is mainly for the sake of characterization, because the focal point resulting from multiple slits has a much higher energy than that from a single slit. Furthermore, it is preferred to employ circularly polarized light $\left(E = \mathrm{e}^{\mathrm{i}(l+\sigma)\phi}\left(\vec{e}_r + \mathrm{i}\sigma\vec{e}_\phi\right)\right)$ to illuminate the semi-ring slits, because it carries a uniformly distributed radial electric field along the azimuthal direction. Note that σ represents the handedness of the circular polarization (1 for right-handed and −1 for left-handed). This allows us to uniformly excite SPPs along the slit, and it is more stable compared with the radially polarized beam. Both spin angular momentum (SAM) and OAM can lead to the phase difference along curved gratings.[37–40] However, the modulation depth achieved by OAM can be much larger than the spin angular momentum (SAM). Although SAM and OAM have quite different physical origins, they arrive at the similar observation—transverse focal point shifts. As a result, when the vortex beams are circularly polarized, these two strategies will couple together to have a superimposed phenomenon:

$$U(\vec{r}) = \int_{-\pi}^{0} \exp(\mathrm{i}j\phi)\frac{\exp(\mathrm{i}k_{\mathrm{SPP}}|\vec{R}-\vec{r}|)}{\sqrt{|\vec{R}-\vec{r}|}}\mathrm{d}\phi, \quad (3)$$

$$x_j = \mathrm{sgn}(j)\frac{\chi_j}{k_{\mathrm{SPP}}}, \quad (4)$$

where $j = \sigma + l$ is the total angular momentum. Given that the total angular momentum is $j = \sigma + l = -1 + l = 0, 1, 2, 3, 4$, a vortex beam with $l = 1$ will be focused at the original point O. As a result, total angular momentum j counts when calculating the transverse focal point shift in this case. This serves as one example of observed equivalence of OAM and SAM.[41–43] Since the circular polarization state of incident light can be

fixed (*e.g.* $\sigma = -1$) in real applications, the total angular momentum is only dependent on the OAM ($j = l - 1$). So the SAM[39,40] can be regarded as a dc-component which determines the focal point position of the case $l = 0$. Therefore, this will not affect the function of OAM discrimination as reported in this work.

Fig. 3a illustrates the sorting sketch of the proposed semi-rings. A Laguerre–Gaussian (LG) beam with circular polarization is employed to illuminate the semi-ring structure from the quartz substrate side to uniformly excite SPPs along the slits. Periodic semi-rings (period P = 600 nm) milled into a 200 nm-thick gold film on the quartz substrate contain five 300 nm-width air-slits to match the plasmon wavelength at an illuminating wavelength of λ = 633 nm, such that a normally incident beam can excite surface waves. Imprinted with a helical phase having a topological charge of l, the surface waves can constructively interfere with each other and finally form a confined spot with a spatial position dependent on l, as shown in Fig. 3a. In our fabricated sample, whose SEM image is shown in Fig. 3b, the inner and outer radii of the smallest slit are 7.85 μm and 8.15 μm, respectively.

Fig. 4a depicts the experimental setup used to characterize the structure (see the NSOM characterization section for details). Fig. 4b shows the NSOM-measured intensity profiles for different LG beams with topological charges l = 1, 2, 3, 4, 5, showing clear hotspots as expected. Line-scanned intensity profiles along the base demonstrate the spatial shifts for different OAM modes, as shown in Fig. 4c. Interestingly, there is no side band intensity detected by NSOM which seems to be a discrepancy compared with that of our theoretical model. However, according to Fig. 1S in the ESI,† it can be explained. The reason is that the limited sensitivity and resolution of our NSOM tip may contribute to this discrepancy. Furthermore, the imperfect structure (fabrication issues) will also degrade the performance. Somehow this discrepancy is even an additional advantage, because it helps to reduce the channel crosstalk. In addition, the measured interval between any two neighboring OAM modes is around 120 nm in Fig. 4d, which coincides with the theoretical value. Illumination of the linearly polarized LG beam can further demonstrate our analytical model. Detailed experimental data can be found in Fig. 2S in the ESI.† However, the linearly polarized LG beam is unfavorable in practice since it will break the one-to-one relation between OAM modes and focal points.

We also investigate its stability for semi-rings with different geometries, *i.e.*, the number of slits and size of the inner slit, to show the robustness of our OAM nano-sorter. Without loss of generality, we take the case of l = 3 for illustration and carry out the simulations in FDTD. In Fig. 5, we can see that the variation of geometry does not influence the spatial shifts of the hotspots, which implies a great stability. However, the increment of slit number enhances the intensity of the hotspots, while this enhancement tends to saturate because of the larger propagation loss of SPPs for the larger-radius semi-ring slits (Fig. 5a). On the other hand, by enlarging the radius of the slits and keeping the ring number fixed, we observe that the intensity of the focal point decreases monotonously (Fig. 5b). From the viewpoint of experiment, the LG beam has a donut-shaped intensity profile and its beam radius increases

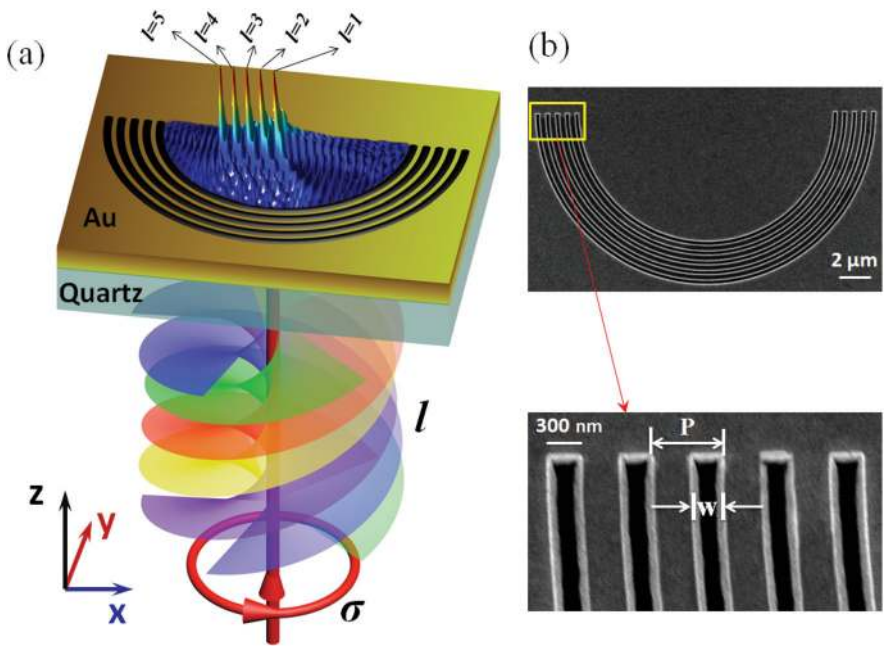

Fig. 3 (a) Schematic of launching and sorting multiplexed LG beams. Mixed orders of circularly polarized (σ = –1) LG beams lead to multiple focal points along a direction radial to the slits whose positions are determined by their topological charge l. (b) SEM image of the nano-sorter and the geometric parameters of the structure. The thickness of the Au layer is 200 nm. The period of the nanoslit is P = 600 nm, and the width is w = 300 nm.

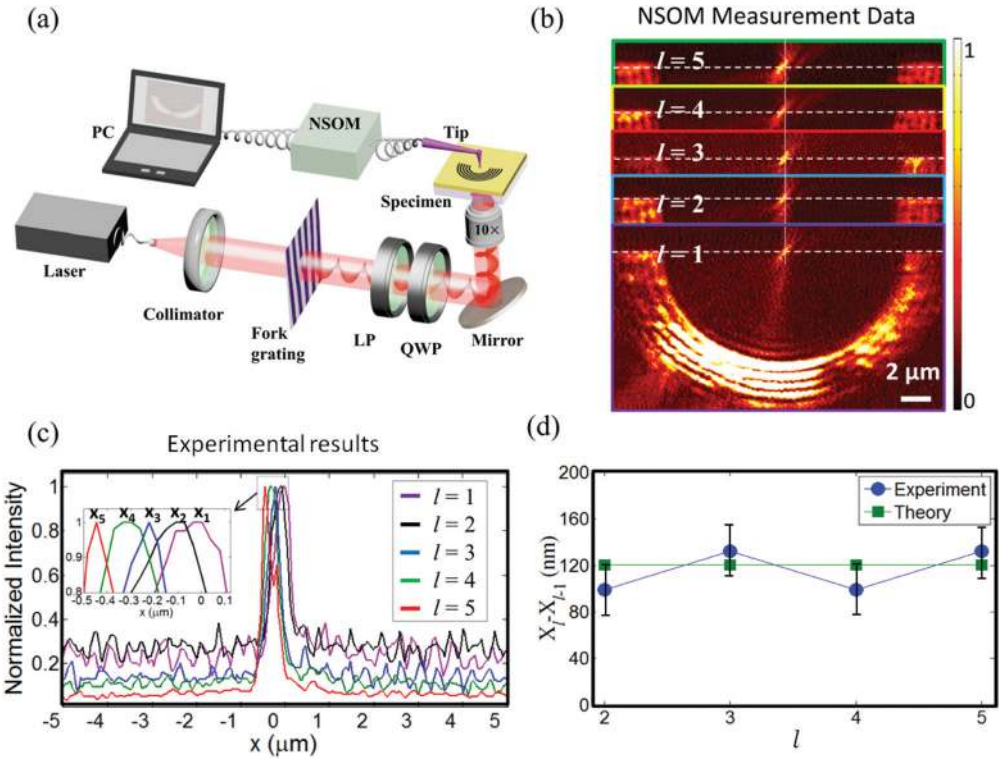

Fig. 4 Characterization of the nano-sorter. (a) Experimental setup. HWP: half waveplate, QWP: quarter waveplate. (b) NSOM images of focusing positions for l = 1, 2, 3, 4, 5. The vertical white solid line is aligned to the focusing position of the state of l = 1. (c) Experimental results of the intensity distributions of different OAM modes along the base (the white dashed lines in (b)) of the slits. (d) Comparison of the measured and theoretical interval between any two neighboring OAM modes, the error bar is mainly caused by the diameter of the NSOM tip.

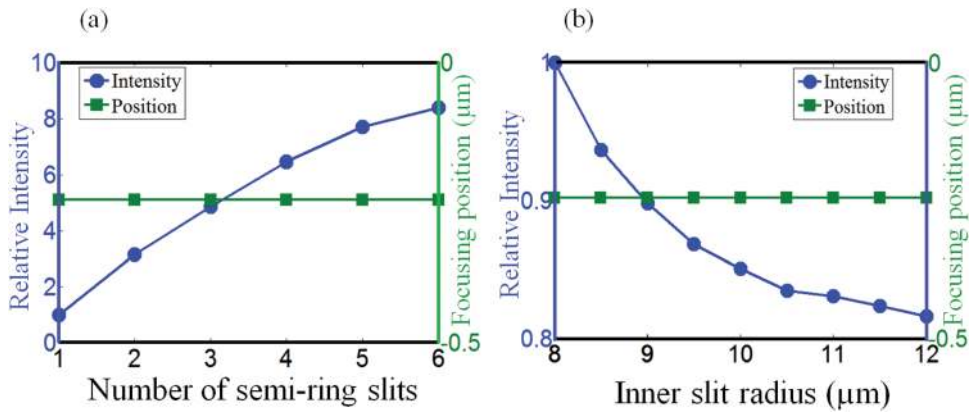

Fig. 5 Simulation of the effect of increasing the number of semi-ring slits and inner slit radius on the focal point's intensity and position (the topological charge of the OAM carried by the incident left-handed circularly polarized plane wave is 3). (a) Effect of the number of slits. The inner slit's radius is fixed at 8 μm. (b) Effect of the semi-ring (inner) slit's radius. The total number of the slits is fixed at 5. The inner slit's radius is from 8 μm to 12 μm.

with l. Therefore, multi-slits (five is used in our nano-sorter) are preferred, which enable the focused LG beam to overlay the slits. This immunity to semi-ring geometry makes the discrimination more reliable.

As derived in eqn (4), the bigger the working wavelength is, the larger the interval between the neighboring two modes will be. In our case, the 120 nm interval corresponds to 633 nm incident wavelength, and it will go to 200–400 nm when considering the near infrared communication band, which would be easier to separate different modes. In particular, the analytical model results of the working wavelength λ = 1.55 μm are presented in Fig. 3S in the ESI† which show 310 nm intervals.

The calculated crosstalk between the neighboring main bands of OAM modes in the current case is about −5 dB (refer to the ESI† for the definition of the crosstalk). On the other hand, interval modes are always suggested instead of consecutive modes, which can largely reduce the crosstalk. For example, l = 1, 4, 7, 10 (or even bigger mode interval[5,7]) will be used as the OAM modes to enhance the system capacity. Under these conditions, the crosstalk will be reduced to −12.1 dB. In addition, analysis of insertion loss of our device can be found in the ESI.† In addition, we are trying to focus different OAM modes into hotspots with a half-round structure rather than receiving them by using a detector with a size-limited aperture, so the singular point in the middle of the vortex beams is no longer our concern. Besides, we are inclined to align the incident beam, which is always required in most nano-devices. Slant incident modes, which are possible to be rectified before the sorter, are not considered here.

The main limitation of this device is that the separation of neighboring OAM modes is relatively small although it is still within the range of resolvability. Future work of increasing the modes' shift may find its solution by employing subwavelength groove waveguides to guide different modes' hot spots away from the rings' center. To be more specific, groove waveguides with a period of 120 nm can be etched coinciding with the positions of the hot spots. Then the energy of the hot spots can be guided along the waveguides, which can be easily separated (Fig. 4S in the ESI†). Another potential strategy of improving the performance is making a raised surface in the vicinity of the structure's center. This raised surface can serve as an amplifier to enlarge the space between different modes. However it may increase the fabrication complexity. In addition, based on the same scheme, it is possible to achieve out-of-chip mode sorting (far field sorting) by implementing slits with a much larger width based on a similar principle, which will also increase the separation.

In conclusion, we have theoretically and experimentally demonstrated the nano-scale separation of OAM of light by a plasmonic nano-sorter composed of semi-ring shaped slits. The significant sorting interval of 120 nm between the neighboring OAM modes might open a new door to the nano-scale discrimination and manipulation of quantum modes of light. The proposed mechanism based on the constructive interference of a phase-modulated surface wave is also useful for general wavefront engineering, which may lead to wide benefits across fields of plasmonic optics, integrated optics and nano-photonics.

NSOM characterization

The experimental characterization of our OAM nano-sorter is implemented to map the electric field at the surface of a gold film by using a fiber tip-type near-field scanning optical microscope (NSOM, NT-MDT NTEGRA Solaris), as sketched in Fig. 4a. The linearly polarized excitation beam originates from a He–Ne laser of wavelength λ = 632.8 nm (MellesGriot, 25-LHP-925-230). A half-wave plate is utilized to rotate the polarization orientation of the laser beam after the light is emitted out from the laser, then illuminated on holographic fork gratings to create a vertical phase with topological charge l = 1–5. The 1st diffraction order of the transmission beams is then selected, and a plano-convex lens with 200 mm focal length is used to collimate the vortex beam which creates a doughnut-shaped cylindrical light beam 1 mm in diameter. Subsequently, the beam passes through a quarter wave plate that can provide left- and right-circular polarization states. The beam is then focused onto the semi-ring shaped nano-sorter at normal incidence, with the beam spot exactly overlapping the nano-sorter pattern, from the substrate side, by an objective lens (Olympus, UPlanFL 10×, NA = 0.3). The near-field SPP distribution is obtained by raster scanning the sample surface with an aperture fiber probe 50 nm in diameter. The distance between the fiber tip and the sample surface is maintained at a few tens of nanometers, which is controlled by a shear-force feedback mechanism. The signal collected by the aperture probe fiber is then guided into a photomultiplier tube (PMT) for recording and amplification.

Acknowledgements

This research is supported by the National Research Foundation, Prime Minister's Office, Singapore under its Competitive Research Programme (CRP Award No. NRF-CRP10-2012-04). C.W.Q. also acknowledges support under the grant R-263-000-A45-112 from the National University of Singapore. The work is also partially supported by the Agency for Science, Technology and Research (A*STAR) under Grant Numbers 0921540099 and 1021740172. We appreciate the stimulating discussions and suggestions with Prof. Erez Hasman about our on-chip discrimination of OAM states.

References

1 L. Allen, M. W. Beijersbergen, R. J. C. Spreeuw and J. P. Woerdman, *Phys. Rev. A*, 1992, **45**, 8185–8189.
2 A. C. Dada, J. Leach, G. S. Buller, M. J. Padgett and E. Andersson, *Nat. Phys.*, 2011, **7**, 677–680.
3 R. Fickler, R. Lapkiewicz, W. N. Plick, M. Krenn, C. Schaeff, S. Ramelow and A. Zeilinger, *Science*, 2012, **338**, 640–643.
4 G. Gibson, J. Courtial, M. J. Padgett, M. Vasnetsov, V. Pas'ko, S. M. Barnett and S. Franke-Arnold, *Opt. Express*, 2004, **12**, 5448–5456.
5 J. Wang, J. Y. Yang, I. M. Fazal, N. Ahmed, Y. Yan, H. Huang, Y. X. Ren, Y. Yue, S. Dolinar, M. Tur and A. E. Willner, *Nat. Photonics*, 2012, **6**, 488–496.
6 N. Bozinovic, Y. Yue, Y. X. Ren, M. Tur, P. Kristensen, H. Huang, A. E. Willner and S. Ramachandran, *Science*, 2013, **340**, 1545–1548.
7 H. Huang, G. D. Xie, Y. Yan, N. Ahmed, Y. X. Ren, Y. Yue, D. Rogawski, M. J. Willner, B. I. Erkmen, K. M. Birnbaum,

S. J. Dolinar, M. P. J. Lavery, M. J. Padgett, M. Tur and A. E. Willner, *Opt. Lett.*, 2014, **39**, 197–200.
8 J. E. Goell and R. D. Standley, *Pr. Inst. Electr. Elect.*, 1970, **58**, 1504.
9 R. C. Alferness, *IEEE J. Quantum Electron.*, 1981, **17**, 946–959.
10 D. G. Hall, *Opt. Eng.*, 1984, **23**, Sr72–Sr72.
11 L. B. Soldano and E. C. M. Pennings, *J. Lightwave Technol.*, 1995, **13**, 615–627.
12 X. L. Cai, J. W. Wang, M. J. Strain, B. Johnson-Morris, J. B. Zhu, M. Sorel, J. L. O'Brien, M. G. Thompson and S. T. Yu, *Science*, 2012, **338**, 363–366.
13 H. Liu, M. Q. Mehmood, K. Huang, L. Ke, H. P. Ye, P. Genevet, M. S. Zhang, A. Danner, S. P. Yeo, C. W. Qiu and J. H. Teng, *Adv. Opt. Mater.*, 2014, **2**, 1193–1198.
14 Y. Gorodetski, N. Shitrit, I. Bretner, V. Kleiner and E. Hasman, *Nano Lett.*, 2009, **9**, 3016–3019.
15 N. Shitrit, S. Nechayev, V. Kleiner and E. Hasman, *Nano Lett.*, 2012, **12**, 1620–1623.
16 D. M. Lin, P. Y. Fan, E. Hasman and M. L. Brongersma, *Science*, 2014, **345**, 298–302.
17 M. Q. Mehmood, C.-W. Qiu, A. Danner and J. Teng, *J. Mol. Eng. Mater.*, 2014, **02**, 1440013.
18 M. Q. Mehmood, H. Liu, K. Huang, S. Mei, A. Danner, B. Luk'yanchuk, S. Zhang, J. Teng, S. A. Maier and C.-W. Qiu, *Laser Photonics Rev.*, 2015, **9**, 674–681.
19 J. Leach, M. J. Padgett, S. M. Barnett, S. Franke-Arnold and J. Courtial, *Phys. Rev. Lett.*, 2002, **88**, 257901.
20 M. P. J. Lavery, A. Dudley, A. Forbes, J. Courtial and M. J. Padgett, *New J. Phys.*, 2011, **13**, 093014.
21 E. Karimi, B. Piccirillo, E. Nagali, L. Marrucci and E. Santamato, *Appl. Phys. Lett.*, 2009, **94**, 231124.
22 G. C. G. Berkhout, M. P. J. Lavery, J. Courtial, M. W. Beijersbergen and M. J. Padgett, *Phys. Rev. Lett.*, 2010, **105**, 153601.
23 G. C. G. Berkhout, M. P. J. Lavery, M. J. Padgett and M. W. Beijersbergen, *Opt. Lett.*, 2011, **36**, 1863–1865.
24 M. P. J. Lavery, D. J. Robertson, G. C. G. Berkhout, G. D. Love, M. J. Padgett and J. Courtial, *Opt. Express*, 2012, **20**, 2110–2115.
25 M. N. O'Sullivan, M. Mirhosseini, M. Malik and R. W. Boyd, *Opt. Express*, 2012, **20**, 24444–24449.
26 M. P. J. Lavery, D. J. Robertson, A. Sponselli, J. Courtial, N. K. Steinhoff, G. A. Tyler, A. E. Wilner and M. J. Padgett, *New J. Phys.*, 2013, **15**, 013024.
27 M. Mirhosseini, M. Malik, Z. M. Shi and R. W. Boyd, *Nat. Commun.*, 2013, **4**, 2781.
28 M. Malik, M. Mirhosseini, M. P. J. Lavery, J. Leach, M. J. Padgett and R. W. Boyd, *Nat. Commun.*, 2014, **5**, 3115.
29 W. H. Zhang, Q. Q. Qi, J. Zhou and L. X. Chen, *Phys. Rev. Lett.*, 2014, **112**, 153601.
30 A. P. Liu, X. Xiong, X. F. Ren, Y. J. Cai, G. H. Rui, Q. W. Zhan, G. C. Guo and G. P. Guo, *Sci. Rep.*, 2013, **3**, 2402.
31 P. Genevet, J. Lin, M. A. Kats and F. Capasso, *Nat. Commun.*, 2012, **3**, 1278.
32 T. H. Su, R. P. Scott, S. S. Djordjevic, N. K. Fontaine, D. J. Geisler, X. R. Cai and S. J. B. Yoo, *Opt. Express*, 2012, **20**, 9396–9402.
33 Z. W. Liu, J. M. Steele, W. Srituravanich, Y. Pikus, C. Sun and Z. X, *Nano Lett.*, 2005, **5**, 1726–1729.
34 L. L. Yin, V. K. Vlasko-Vlasov, J. Pearson, J. M. Hiller, J. Hua, U. Welp, D. E. Brown and C. W. Kimball, *Nano Lett.*, 2005, **5**, 1399–1402.
35 V. Y. Bazhenov, M. V. Vasnetsov and M. S. Soskin, *JETP Lett.*, 1990, **52**, 429–431.
36 V. Y. Bazhenov, M. S. Soskin and M. V. Vasnetsov, *J. Mod. Opt.*, 1992, **39**, 985–990.
37 A. Acs CatalysisNiv, G. Biener, V. Kleiner and E. Hasman, *Opt. Lett.*, 2005, **30**, 2933–2935.
38 A. Niv, G. Biener, V. Kleiner and E. Hasman, *Opt. Lett.*, 2007, **32**, 847–849.
39 K. Y. Bliokh, Y. Gorodetski, V. Kleiner and E. Hasman, *Phys. Rev. Lett.*, 2008, **101**, 030404.
40 Y. Gorodetski, A. Niv, V. Kleiner and E. Hasman, *Phys. Rev. Lett.*, 2008, **101**, 043903.
41 E. Brasselet, Y. Izdebskaya, V. Shvedov, A. S. Desyatnikov, W. Krolikowski and Y. S. Kivshar, *Opt. Lett.*, 2009, **34**, 1021–1023.
42 E. Brasselet, G. Gervinskas, G. Seniutinas and S. Juodkazis, *Phys. Rev. Lett.*, 2013, **111**, 113901.
43 D. Hakobyan and E. Brasselet, *Nat. Photonics*, 2014, **8**, 610–614.